Phase-field modelling of electromigration-induced intergranular slit propagation in metal interconnects

Arnab Mukherjee [a,b,*], Kumar Ankit [c], Michael Selzer [a,b], Britta Nestler [a,b]

[a] Institute for Digital Materials Science (IDM), Karlsruhe University of Applied Sciences, Moltkestr. 30, 76133, Karlsruhe, Germany

[b] Institute of Applied Materials (IAM-MMS), Karlsruhe Institute of Technology, Strasse am Forum 7, 76131, Karlsruhe, Germany

[c] Materials Science and Engineering, School for Engineering of Matter, Transport, and Energy, 551 E. Tyler Mall, Arizona State University, Tempe, AZ 85287-6106, USA

Keywords:
Electromigration
Phase-field method
Grain-boundary grooving
Slit propagation

A B S T R A C T

We use a phase-field method to elucidate grain-boundary grooving as a mechanism of genesis and subsequent propagation of intergranular slit in metal interconnects under concurrent surface and grain boundary diffusion. Surface diffusion is assumed to be the rate limiting transport mechanism. Accelerated grain-boundary grooving induced by electromigration is shown to ensue a narrow channel-like slit which advances at a steady state along the grain-boundary preserving its shape near the tip region. The slit characteristics namely the width and velocity dependence on electric field derived are shown to be in excellent agreement with the sharp interface calculations which treat the tip region of the slit independently. Furthermore, the simulations reveal that for the same magnitude of electric field, a slit conceived from a smaller grain exhibits a slower kinetics and delay damage dissemination. The apparent discrepancy from the sharp interface description is resolved on the basis of curvature gradient and electromigration-induced surface flux which heal the root during groove to slit transition and is predominant in smaller grains. Finally, drawing analogy from the nucleation and growth models of electromigration voids, failure due to intergranular slit is divided into serial process of initial grooving followed by slit propagation stage. The lifetime analysis suggests the grooving stage to be the rate determining step in the failure process, yielding an exponent of 1.33 in Black's law.

1. Introduction

Passage of electric current across a metal conductor instigates an "electron wind", which imparts momentum to the metal ions thereby ensuing atomic diffusion in the direction of electron flow. The phenomenon, known as electromigration (EM), raises serious reliability concern in modern integrated circuits [1–3]. EM damage in thin films has garnered much attention due to its implication in efficient designing of interconnects [4,5].

Experimental observations suggest that the damage typically commences at microstructural heterogeneous sites such as grain boundaries (GB) [6], triple junctions [7], metal–dielectric interfaces at the passivation layer and sidewalls [8] or at the intersection of GBs with a free surface due to non-vanishing divergence of flux. A negative flux divergence results in mass accumulation in form of hillocks leading to short circuit between neighbouring vias [9]. While, a positive flux divergence initiates voids due to material depletion [10]. The voids can migrate along the line preserving its shape or evolve into various time dependent configurations [11,12]. Perhaps, the most pervasive form of failure is the transition of migrating voids into finger or channel like slits [13–15]. Depending upon the propagation path, the slits, can be classified as transgranular advancing through the grains [16,17] or intergranular that are localized along the GBs [18]. Slits have also been known to result from surface roughness or perturbations at the edge of the line [12,13,19].

Accelerated GB grooving represents another viable mechanism through which slits manifest at external surfaces, passivation layer or GB triple junctions [7,20]. While slits evolving from voids require availability of heterogeneous sites for nucleation of void, those conceived from GB grooving can occur without any nucleation event [7]. The preclusion of nucleation implies that the damage induced by GB grooving will proceed at any level of vacancy accumulation. The phenomenon is further exacerbated in wide polycrystalline line where once a slit originates from a GB groove, subsequent propagation is rapid along the line owing to contiguous GB network [6,21]. Slits have also been observed in bamboo type lines emerging from side walls and propagating transverse to the line along a tilted GB [8,22].

* Corresponding author at: Institute of Applied Materials (IAM-MMS), Karlsruhe Institute of Technology, Strasse am Forum 7, 76131, Karlsruhe, Germany.
E-mail address: arnab.mukherjee3@partner.kit.edu (A. Mukherjee).

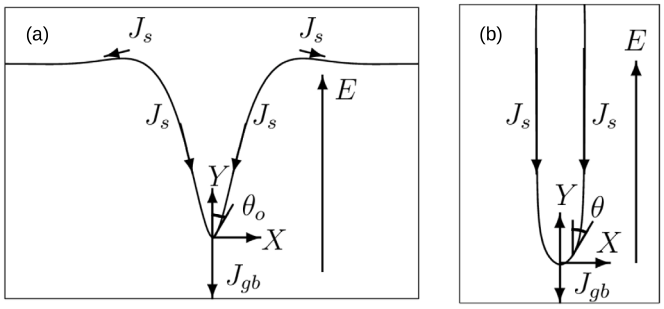

Fig. 1. (a) Schematic illustration of the early stages of grain boundary grooving under electromigration. The GB flux, J_{gb} drains the material out of the GB, causing groove extension, while the surface flux, J_s, transports material to the groove root to maintain the dihedral angle θ_o. (b) Higher J_{gb} eventually localizes the groove to form a channel-like slit propagating along the GB. E is the applied electric field and θ the surface tangent.

While slits originating from voids and edge perturbations due to surface EM have been studied extensively [12,13,19,23,24], investigations on the role of intergranular slits as a damage mode remain few [8,22,25]. The present work elucidates GB grooving as a mechanism of genesis and propagation of intergranular slit under concurrent surface and grain boundary diffusion. Surface diffusion is assumed to be the rate limiting transport mechanism. Though seemingly impractical, surface diffusion can be significantly inhibited due to the presence of oxides and contaminants as reported in [26,27]. GBs in such cases emerge as the dominant EM pathway especially in wide polycrystalline lines [28].

The present article is organized as follows. In the next section we describe the sharp interface relation of the physical problem followed by the phase-field description of the same. Thereafter, the phenomenon of groove to slit transition is investigated in Section 4 and critically compared to those from sharp interface relations. We conclude the article by a brief discussion regarding the implication of the results and possible extensions in Section 5.

2. Sharp-interface relations

We briefly recall the sharp interface relations which might be useful in benchmarking and interpreting the results derived from the phase-field method. Moreover, the analytical calculations made in this section are based on certain simplifying assumptions to make the problem mathematically amenable, some of which will be relaxed in the phase-field simulations.

Whenever a GB intersects a free surface, grooves develop at the surface-GB intersection as a result of the system trying to attain the equilibrium dihedral angle, resulting in the reduction of GB, while expelling material onto the surface. This instigates curvature gradients along the surface which further provides the impetus for mass flux [29]. The presence of external field such as applied stress or electric field as in the present study, induces a GB flux which drains matter out of the GB, additionally providing a driving force for GB reduction [7,30].

It was shown by Mullins that the governing partial differential equation (PDE), describing the evolution of the surface under the small slope approximation (SSA) can be written as [29],

$$\frac{\partial y}{\partial t} = -By'''' \tag{1}$$

where, B is a material parameter given by,

$$B = \frac{D_S \gamma_S \Omega^2 \nu_S}{k_B T} \tag{2}$$

where, D_S is the surface diffusivity, γ_S the surface energy, Ω the atomic volume, ν_S the number of surface atoms per unit area, k_B the Boltzmann constant and T the temperature. The above PDE is solved under the following initial (IC) and boundary conditions (BC) [7,29,30],

(i) the initial surface is flat i.e.

$$y(x,0) = 0 \tag{3}$$

(ii) constant slope at the root, which under the SSA translates into,

$$y'(0,t) = m = \tan(90-\theta_o) \approx \sin(90-\theta_o) = \gamma_{GB}/2\gamma_S \tag{4}$$

(iii) the continuity of the flux at the root,

$$J^{rt}_{GB} = 2J^{rt}_{S}, \tag{5}$$

$$\frac{D_{GB}\nu_{GB}Z_{GB}eE_o}{k_BT} = \frac{2D_S\gamma_S\Omega\nu_S}{k_BT}\frac{\partial^3 y}{\partial x^3}, \tag{6}$$

$$y'''(0,t) = \frac{J^{rt}_{GB}\Omega}{2B} = I. \tag{7}$$

D_{GB} denotes the GB diffusivity, γ_{GB} the GB energy, ν_{GB} the number of GB atoms per unit area, Z_{GB} the effective valence of atom at GB, e the electron charge and E_o the applied electric field. Eq. (1) can be solved using standard methods such as laplace transform suggested by Mullins. Alternatively, the solution can also be derived employing cosinus transform [31]. The basic solution step involves taking a laplace transform in time or cosinus transform in spatial variables to convert the partial differential equation to an ordinary differential equation (ODE). The ODE is then solved using the IC and BCs (3), (4) and (5) and applying inverse transform to obtain the solution at the root as [7,30],

$$y(0,t) = -\frac{m(Bt)^{1/4}}{\sqrt{2}\Gamma(5/4)} + \frac{I(Bt)^{3/4}}{\sqrt{2}\Gamma(7/4)}. \tag{8}$$

The former term of the above expression describes the groove evolution solely under capillary-induced surface diffusion. While, the latter reflects the contribution arising due to the presence of external field. The general solution of the PDE (1) can be written as [30],

$$y(x,t) = m(Bt)^{1/4}Z[x/(Bt)^{1/4}] + I(Bt)^{3/4}W[x/(Bt)^{1/4}], \tag{9}$$

where $Z(u)$ and $W(u)$ are power series of the form $\sum_{n=0}^{\infty} a_n u^n$. It is worth noting that the slope of the profile ($y'(x,t)$) exhibits a $t^{1/2}$ dependence due to external field-induced term. As a result, the groove is expected to become steeper with time until SSA is no longer valid. Eventually, the external field will localize the groove to form a channel-like slit which, thereafter, propagates along the GB.

Once the slit forms, it can be analysed independently as in the case of cavity growth problems [32]. The slit shape is assumed to be parabolic at the tip while maintaining the equilibrium dihedral angle. The slit surface is assumed flat further from the tip as shown in Fig. 1(b). The GB flux J_{GB} and the surface flux J_S in the flat portion of the slit arise only due to the presence of electric field and can be expressed as [22,25],

$$J_{GB} = \frac{D_{GB}\delta_{GB}Z_{GB}eE_o}{\Omega k_BT}, \tag{10}$$

$$J_S = \frac{D_S\delta_S Z_S eE_o}{\Omega k_BT}. \tag{11}$$

Z_S denotes the effective valence of the species at the surface. δ_S and δ_{GB} are the thickness of the surface and GB layer related the number of surface and GB atoms as $\nu_S = \delta_S/\Omega$ and $\nu_{GB} = \delta_{GB}/\Omega$. The flux at any point along the curved portion of the slit surface can be written as a sum of the contributions arising from capillarity and electric field as,

$$J = \frac{D_S\delta_S}{\Omega k_BT}\left[-\Omega\gamma_S\frac{d\kappa}{ds} + Z_S eE_o\cos\theta\right]. \tag{12}$$

Using the relations, $\kappa = d\theta/ds$, $dX/ds = \sin\theta$ and substituting $F = \cos\theta$, in the above expression yields,

$$J = \frac{D_S\delta_S}{\Omega k_BT}\left[-\sqrt{1-F^2}\Omega\gamma_S\frac{d^2F}{dX^2} + Z_S eE_o F\right]. \tag{13}$$

The mass conservation along the slit surface relates the flux to the normal velocity V_n as,

$$\frac{dJ}{ds} = -\frac{V_n}{\Omega}. \tag{14}$$

The mass balance equation relates the slit velocity to the fluxes as,

$$V = (J_{GB} - 2J_S)/2h, \tag{15}$$

where $2h = w$ is the slit width.

Using the above relations and $V_n = V\sin\theta$, integrating the above equation and determining the integration constant utilizing the condition that at $X = 0$, $J = J_{GB}/2$ we arrive at,

$$(J_{GB} - 2J_S)\frac{X}{h} = J_{GB} - 2J. \tag{16}$$

Inserting the relations (10), (11) and (13) and rearranging we get,

$$\frac{2D_S\delta_S\gamma_S}{k_BT}\sqrt{1-F^2}\frac{d^2F}{dX^2} + J_{GB}(\frac{X}{h} - 1) + 2J_S(F - \frac{X}{h}) = 0 \tag{17}$$

Non-dimensionalizing the above expression by introducing $\overline{X} = X/h$ and dividing throughout by $2J_S$ yields,

$$A\sqrt{1-F^2}\frac{d^2F}{d\overline{X}^2} + (F - \overline{X}) + M(\overline{X} - 1) = 0, \tag{18}$$

where,

$$A = \frac{\gamma_S\Omega}{Z_S e E_o h^2}, \tag{19}$$

$$M = \frac{D_{GB}\delta_{GB}Z_{GB}}{2D_S\delta_S Z_S}. \tag{20}$$

Owing to the highly non-linear nature of the governing PDE, (18) is solved numerically subjected to the BC $F = \cos\theta_o$ at $\overline{X} = 0$ and $F = 1$, $dF/d\overline{X} = 0$ at $\overline{X} = 1$. The numerical solution was obtained by Klinger et al. [25] and hence we do not delve further in this direction. However, certain key points and limitations in the sharp interface description of the problem needs to be highlighted.

(i) Firstly, the solution given by Eq. (9) describes the surface evolution faithfully only at the early stages when the slope at the root is small. However, as mentioned the SSA will eventually be violated. It is also worth noting that Eq. (9) pertains to the evolution of the entire surface and not only of the root. As a result, groove to slit transition will never be predicted under the SSA.

(ii) Secondly, while applying flux continuity at the root (Eqs. (5) and (6)), the EM-induced surface flux has been neglected in RHS of Eq. (6). As grooving progresses, the freshly exposed surfaces come in contact with the electron wind force, thus engendering an additional contribution to the surface flux. EM-induced surface flux is time dependent (because the groove profile is continuously changing) and hence the assumption of constant flux I in Eq. (7) is expected to be true only during early stages when this contribution is marginal.

(iii) Thirdly, the dynamics of the slit stage is calculated independently (i.e. starting from a pre-existing crack) without considering the initial grain size from which it is conceived. In other words, this implies that for the same magnitude of electric field, the slit characteristics namely the width and velocity is independent of the grain size.

(iv) Electric field is assumed to be constant along the flat part of the slit surface and approximated with a simple projection in the vicinity of the tip. In reality, however, sharp corners and edges lead to enhanced localized field, a phenomenon known as field crowding.

The principle aim of the present work is to investigate the initiation and propagation of intergranular slit numerically. Besides, owing to the non-linearity of the problem, it is impossible to pursue the complete groove to slit transition analytically. Phase-field method, with the advantage of managing complex topological changes without explicitly tracking the interface, lends as a natural numerical choice to study such moving boundary problems. Moreover, all the above limitations which can severely affect the lifetime of conductors can be addressed duly. The phase-field model is presented in the following section.

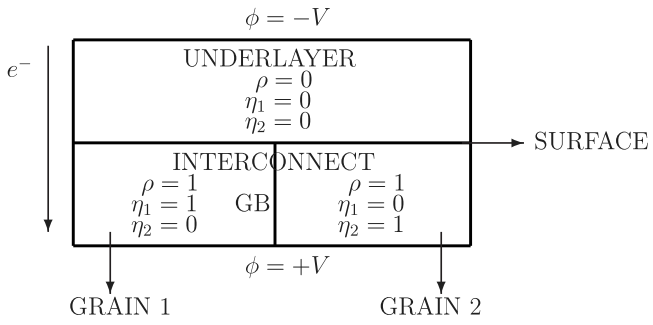

Fig. 2. Schematic of the simulation set-up used in the present study. The interconnect consists of array of periodic grains with GB aligned along the direction of electric field. The upper electrode is assigned a negative potential while the bottom one a positive value. The electron wind is directed towards the bottom electrode.

3. Phase-field formulation

3.1. Model

We seek to construct a simplified model that can correctly capture the diffusion driven EM phenomenon. Following [33–36], we employ a set of conserved and non-conserved order parameters to distinguish between the underlayer and the polycrystalline interconnect domain. The simulation set up is a Blech-type test geometry [37] which comprises of an array of periodic grains of the metal interconnect separated from the dielectric underlayer as shown in Fig. 2. A conserved order parameter, which, in the present case is the scaled density variable ρ, distinguishes the underlayer ($\rho = 0$) and the interconnect ($\rho = 1$) domain. While, a set of N non-conserved order parameters $(\eta_1, \eta_2, \ldots, \eta_N)$ are chosen to describe the multiple grains in the interconnect microstructure. The non-conserved order parameters are chosen such that the ith grain of the interconnect is described by $\eta_i = 1$ and $\eta_j = 0\ \forall\ j \neq i$, where as the underlayer domain is defined by $\eta_i = 0\ \forall\ i \in \{1, 2, \ldots, N\}$.

With the above description, GB is defined as the region between ith and jth grain where η_i and η_j varies smoothly between $0 < \eta_i, \eta_j < 1$. Surface, on the other hand is the region between the underlayer and the ith grain of the interconnect exhibiting smooth variation of ρ and η_i as $0 < \rho, \eta_i < 1$. Using the definition of conserved and non-conserved order parameters the free energy functional is defined as,

$$F = \int_V f(\rho, \eta_i) + \kappa_\rho|\nabla\rho|^2 + \kappa_\eta\sum_{i=1}^{N}|\nabla\eta_i|^2 dV \tag{21}$$

where, κ_ρ and κ_η are the gradient energy coefficients which penalizes gradients in ρ and η respectively. $f(\rho, \eta_i)$ is a Landau-type potential which creates $(N + 1)$ distinct minimas at $(\rho, \eta_1, \eta_2, \ldots, \eta_N) = (1, 1, 0, \ldots, 0), (1, 0, 1, \ldots, 0), \ldots, (0, 0, 0, \ldots, 0)$ in the free energy landscape. The explicit expression of $f(\rho, \eta_i)$ can be derived considering simple symmetry arguments as [33],

$$f(\rho, \eta_i) = A\rho^2(1-\rho)^2 + B\rho^2\xi(\eta_i) + C(1-\rho)^2\sum_{i=1}^{N}\eta_i^2 \tag{22}$$

where the function $\xi(\eta_i)$ is a multiwell in η_i,

$$\xi(\eta_i) = \sum_{i=1}^{N}\left[\frac{\eta_i^4}{4} - \frac{\eta_i^2}{2} + 2\sum_{j>i}^{N}\eta_i^2\eta_j^2\right] + \frac{1}{4}. \tag{23}$$

A, B and C are the energy barrier with units of energy per unit volume. The first term in Eq. (22) results in two degenerate states in ρ, corresponding to the interconnect and the underlayer domain. It is to be noted that the prefactor ρ^2 and $(1-\rho)^2$ in the second and third term alters the free energy landscape in the interconnect and the underlayer domain respectively. The second term in Eq. (22) exhibits N minima in η_i, $(\eta_1, \eta_2, \ldots .., \eta_N) = (1, 0, \ldots .., 0), (0, 1, \ldots .., 0), (0, 0, \ldots .., 1)$ corresponding to various grain orientations in the interconnect defined by $\rho = 1$. The underlayer i.e. $\rho = 0$ is characterized by a single minimum in η_i, $(\eta_1, \eta_2, \ldots .., \eta_N) = (0, 0, \ldots .., 0)$ according to the third term.

The kinetic equations of the conserved and the non-conserved order parameters are obtained from the free energy functional by variational derivatives. Thus, the non-conserved order parameters follow the dynamics of Allen–Cahn Eq. as [38],

$$\frac{\partial \eta_i}{\partial t} = -L\frac{\delta F}{\delta \eta_i} \tag{24}$$

$$= -L\left[\frac{\partial f(\rho, \eta_i)}{\partial \eta_i} - 2\kappa_\eta \nabla^2 \eta_i\right] \tag{25}$$

where, L is the relaxation coefficient for the non-conserved order parameters. The conserved order parameter, on the other hand, is governed by Cahn–Hilliard Eq. as [39],

$$\frac{\partial \rho}{\partial t} = \nabla \cdot M(\rho, \eta_i)\nabla\overline{\mu} \tag{26}$$

where,

$$\overline{\mu} = \mu + ze\phi. \tag{27}$$

The chemical potential μ is defined from the variational derivative as,

$$\mu = \frac{\delta F}{\delta \rho}. \tag{28}$$

z is the effective valence of the diffusing species which according to the sharp interface definition is a sum of direct electrostatic and the wind force contributions. Thus Eq. (26) translates into,

$$\frac{\partial \rho}{\partial t} = \nabla \cdot M(\rho, \eta_i)\nabla(\mu + ze\phi) \tag{29}$$

The above Eq. implies the motion of diffusing species under the combined influence of gradient of chemical potential as well as electric potential. To account for enhanced diffusivities at the surface and GB, the mobility is expressed as a scalar function of ρ and η_i as [33,40],

$$M(\rho, \eta_i) = M_B + 16M_S\rho^2(1-\rho)^2 + 4M_{GB}\sum_{j>i}\sqrt{\eta_i^2\eta_j^2} \tag{30}$$

where M_B, M_{GB} and M_S stands for the atomic mobility in the bulk, at the GBs and at the surface respectively.

Few comments are in order regarding the specific choice of mobility function. The second term in Eq. (30) represents surface diffusion at the interconnect-underlayer interface. ρ by virtue of its conserved nature exhibits the Gibbs–Thomson effect, as a result of which, ρ may overshoot the prescribed limit of $0 < \rho < 1$ depending upon the local curvature. Since we adopt a scalar mobility function (instead of a tensorial form [41,42] which inherently restricts diffusion along the surface), the higher degeneracy specifically suppresses the additional bulk diffusion contribution arising from the local variation of ρ and is able to recover pure surface diffusion limited motion i.e. motion by surface laplacian of the mean curvature as demonstrated via rigorous asymptotic analysis [43]. Moreover, the biquadratic mobility in conjunction with the fact that we investigate interface feature of the order of few nanometers suffices in restricting diffusion currents along the surface and ensures vanishing normal fluxes as will be shown later. Biquadratic mobility also has the attractive feature that it always returns a non-negative value thus obviating any numerical instabilities.

Since the time scale of electrodynamics is much smaller in comparison to the diffusion process, we solve the laplace equation assuming no charge accumulation to evaluate the electrostatic field distribution as,

$$\nabla \cdot \left[\sigma(\rho)\nabla\phi\right] = 0 \tag{31}$$

where σ is the conductivity taken to be ρ dependent to distinguish the electrical property of the metal interconnect and dielectric underlayer. We use a linear interpolation between the interconnect and underlayer as,

$$\sigma(\rho) = \sigma_m\rho + \sigma_u(1-\rho) \tag{32}$$

Thus Eqs. (25), (29) and (31) combines a degenerate Cahn–Hilliard, Allen–Cahn and Laplace Eq. which constitutes coupled PDEs for the electromigration problem. All the quantities are rendered non-dimensional by selecting a characteristic energy scale $E' = A'$, a length scale $L' = \left(\frac{\kappa'_\rho}{A'}\right)^{1/2}$ and a timescale $t' = \frac{L'^2(\rho'_{int}-\rho'_{die})^2}{M'_B E'}$ where ρ'_{int} and ρ'_{die} are the densities of the interconnect and the dielectric underlayer respectively.The interested readers are referred to Ref. [44] for the details of the non-dimensionalization procedure. To avoid confusion, we drop the tildes hereafter.

Table 1
Non-dimensionalized numerical parameters used in the present study and corresponding interfacial properties.

Parameter	Non-dimensional value
κ_ρ	1
κ_η	0.33
A, B, C	1
M_B	10^{-6}
M_{GB}	1
M_S	0.1
ze	−5
σ_m	3
σ_u	0.3
$\Delta x, \Delta y$	0.5
Δt	0.001
γ_S	0.6
γ_{GB}	0.42
δ_S	3.7
δ_{GB}	2.3

3.2. Relation to sharp interface models

We next relate the phase-field parameters to their tradition sharp interface counterparts. The gradient-energy coefficients and the potential well heights in phase-field model can be related to the interfacial energy (γ) and width (δ). The interfacial energy of the present system considering a one dimensional domain, can be written as [38,39],

$$\gamma = \int_{-\infty}^{+\infty} \Delta f(\rho, \eta_i) + \kappa_\rho|\nabla\rho|^2 + \kappa_\eta\sum_{i=1}^{N}|\nabla\eta_i|^2 \mathrm{d}x \tag{33}$$

where $\Delta f(\rho, \eta_i)$ is the excess free energy of the homogeneous system with respect to the free energy of equilibrium two phase system. It can further be shown that at equilibrium, the contribution arising from gradient terms and excess energy are equal so that [39],

$$\gamma = 2\int_{-\infty}^{+\infty} \Delta f(\rho, \eta_i)\mathrm{d}x \tag{34}$$

Though the above integral can be routinely solved analytically for simple quartic potentials, the same is not possible for the potential selected here. Hence, we integrate Eq. (33) numerically to determine the surface (γ_S) and GB (γ_{GB}) energies. To compute γ_{GB}, we start with a planar $1-D$ domain between two grains with their respective equilibrium configuration i.e. $(\rho, \eta_1, \eta_2) = (1, 1, 0)$ and $(1, 0, 1)$. We solve Eqs. (25) and (29) and allow the interfaces to diffuse until no appreciable change is observed between two successive timesteps. Eq. (33) is then integrated numerically to determine γ_{GB}. γ_S is also defined

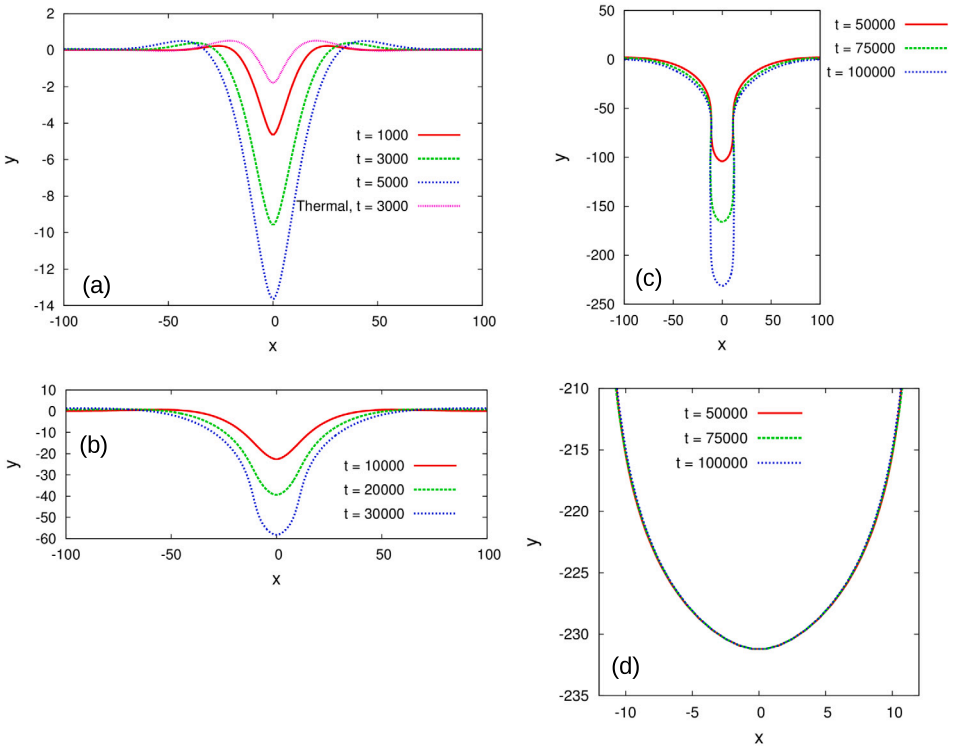

Fig. 3. Groove profiles depicting (a) initial, (b) intermediate and (c) late stages of evolution of a slit from an initial GB groove. The applied electric-field initiates a morphological instability at the triple junction in the form of a narrow channel-like slit, propagating along the grain-boundary. (d) Slit propagates along the GB preserving its shape near the tip region.

along similar lines. Since the interconnect is essentially a pure metal, the parameters $A, B, C, \kappa_\rho, \kappa_\eta$ are selected such that γ_S is greater than γ_{GB}. This is achieved by selecting a higher value of κ_ρ than κ_η. The specific values are reported in Table 1. The interfacial widths (δ_{GB} and δ_S) are defined heuristically as the region where the respective order parameters vary between 0.1 and 0.9.

We next turn our attention towards the kinetic parameters namely the atomic mobilities and the relaxation coefficient. The bulk atomic mobility in phase-field models can be related to the bulk diffusivity by comparing the Cahn–Hilliard Eq. (26) to Fick's law implying

$$D_B = M_B \frac{\partial^2 f}{\partial \rho^2}. \tag{35}$$

The relationship between surface mobility and surface diffusivity can be established by performing a matched asymptotic analysis and comparing the expression for the normal velocity of the interface with the sharp-interface description, yielding, [44]

$$B = \gamma_S \overline{M}_S \tag{36}$$

where $\overline{M}_S = \int_{-\infty}^{+\infty} 16 M_S \rho^2 (1-\rho)^2 \mathrm{d}x$. Similarly, the GB mobility and diffusivity can be related by comparing the GB flux from sharp-interface and phase-field model leading to the expression

$$\frac{D_{GB}\delta_{GB}}{k_B T} = \overline{M}_{GB}, \tag{37}$$

where, $\overline{M}_{GB} = \int_{-\infty}^{+\infty} 4 M_{GB} \sqrt{\eta_i^2 \eta_j^2} \mathrm{d}x$. Since we intend to study surface diffusion limited slit formation, we choose M_{GB} an order of magnitude higher than M_S, while the bulk atomic mobility M_B is set to a very low value of 10^{-6}.

It is worth mentioning that since ρ roughly maintains a constant value across the GB, the motion is governed by the Allen–Cahn equation, but only approximately. Consequently, GB exhibits the standard motion by mean curvature assuming no solute segregation. Accordingly, a comparison of the expression of the interfacial velocity from the classical sharp-interface theories of curvature-driven motion and the phase-field model yields [38],

$$L\kappa_\eta = \mu_{GB}\gamma_{GB} \tag{38}$$

where μ_{GB} is the GB mobility. Physically, the surfaces evolve via the mechanism of surface diffusion. If we look at the construction of the present phase-field model, the surfaces i.e. the interface between underlayer and interconnect are represented by gradients in both ρ and η. Both Cahn–Hilliard and Allen–Cahn equations are solved along these interfaces and the kinetics is determined by the respective kinetic coefficients i.e. M_s for Cahn–Hilliard and L for Allen–Cahn. Both these equations model different physical phenomenon viz. Cahn–Hilliard models motion of surface by atomic diffusion (or more precisely surface laplacian of the curvature in case of surface diffusion) where as Allen–Cahn dictates motion by surface attachment kinetics. To ensure that the motion of the surface is governed by atomic diffusion, the kinetics of Cahn–Hilliard equation needs to be slower (rate limiting step) than Allen–Cahn equation. This can be achieved by setting a value of L such that results are independent of this value. To achieve this property, the value of L is selected to be 1 such that the interface movement is diffusion controlled. The details of the asymptotic analysis of the model and some numerical results regarding the effect of the kinetic parameter L can be found in Ref. [44]

Moving on to the electrical parameters, as mentioned before, the effective valence ze is a resultant of a direct electrostatic and wind force. In most commercial metallic interconnects, the wind force is dominant which implies that z is negative. Moreover, effective valence is also an interfacial property and can assume different values at GB and surfaces. However, in the present work it is assumed to be a constant and we select a representative value of −5. Furthermore, the direction of electron flow is chosen such that there is net EM flux out of the groove root (negative y direction) which is necessary for slit evolution. This is attained by prescribing a negative potential at the top edge and a positive potential at the bottom edge. Following the

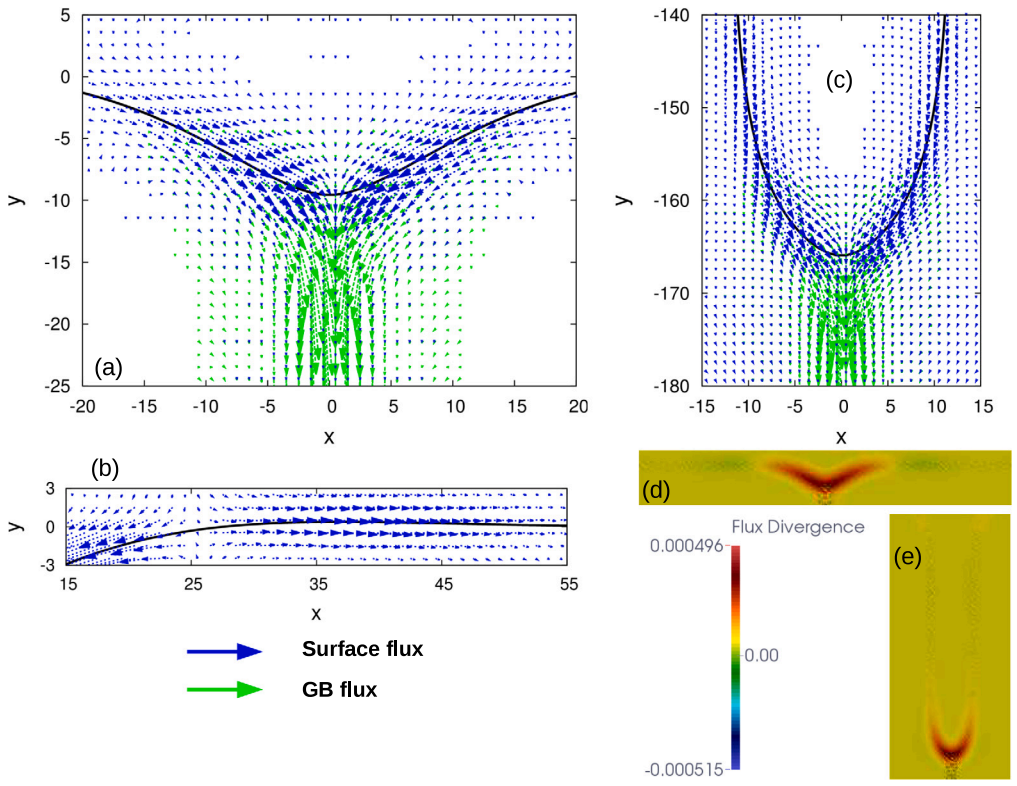

Fig. 4. Vector plots denoting the surface (blue arrow) and GB (green arrow) diffusion currents at (a) the groove root region corresponding to $t = 3000$, (b) the groove tail (surface) corresponding to $t = 3000$ and (c) the slit tip corresponding to $t = 75\,000$. The length of the arrows denotes the magnitude of the respective fluxes which have been upscaled for clarity. Flux density maps at (d) $t = 3000$ and (e) $t = 75\,000$ indicate triple junctions as potential flux divergence sites. A positive flux divergence at the triple junction implies a net outflow of material due to the higher GB atomic mobility in comparison to the surface atomic mobility.

standard electrostatic convention, the electric field is directed towards the positive y axis. The conductivity of the metal interconnect is set to be 10 times higher than the dielectric underlayer. All the simulation parameters are summarized in Table 1.

The governing Eqs. (25) and (29) are solved using explicit finite difference scheme where the spatial derivatives are discretized using a combination of forward, backward and central differences in a staggered grid which is second order accurate. While, the temporal derivatives are discretized using an explicit Euler scheme. Laplace Eq. (31) is solved iteratively using successive-over-relaxation (SOR) method with relaxation parameter of 1.7. The convergence criteria is set such that the maximum difference between successive iterations is less than 10^{-6}. No flux boundary conditions are applied for ρ and η_i at top and bottom edges by prescribing,

$$\hat{n} \cdot \nabla\rho = \hat{n} \cdot M\nabla\mu = \hat{n} \cdot \nabla\eta_i = 0 \tag{39}$$

Periodic boundary conditions are applied at the left and right edges for ρ and η_i. For the potential field ϕ, dirichlet boundary condition are prescribed at top and bottom edges and no flux at left and right edges.

4. Results

A few comments on the general applicability of the results. Firstly, we neglect the effect of back stress along the line. In Blech-type test geometries as the conductor drifts in the direction of electron wind a back stress is generated across the line which impedes the further movement [45]. This essentially implies that the slit evolves and propagates along an infinite GB. Secondly similar to Ref. [19], EM fluxes are not blocked at the domain edges. Consequently, the slit can increase its area, although the mass is locally conserved. Finally, all the properties of the interconnect namely interfacial energy, atomic mobility and the conductivity has been assumed to be isotropic. The

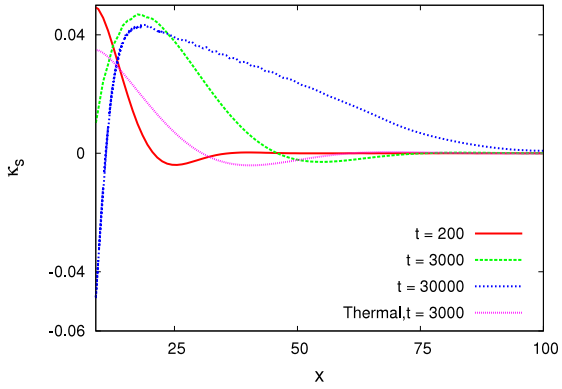

Fig. 5. Variation of the mean curvature κ_s along the surface profile given by $\rho = 0.5$ contour. A transition from a convex (positive) to a concave (negative) curvature at the groove root signifies the initiation of the instability in form of slit.

assumptions, considerably simplifies the analysis, however, we remark, that anisotropy in either of the property can easily be incorporated and is not a limitation of the phase-field modelling in general. Anisotropy in atomic mobility can have marked influence on the slit propagation dynamics as reported in previous works concerning single crystals [13, 19,23,24].

4.1. GB slit propagation : Role of surface and GB

To begin with, we consider the morphological evolution of surface diffusion limited grooves under the concomitant influence of capillarity and EM. The temporal evolution of surface defined as the $\rho = 0.5$ level set is presented in Fig. 3. Three distinct regimes can be observed

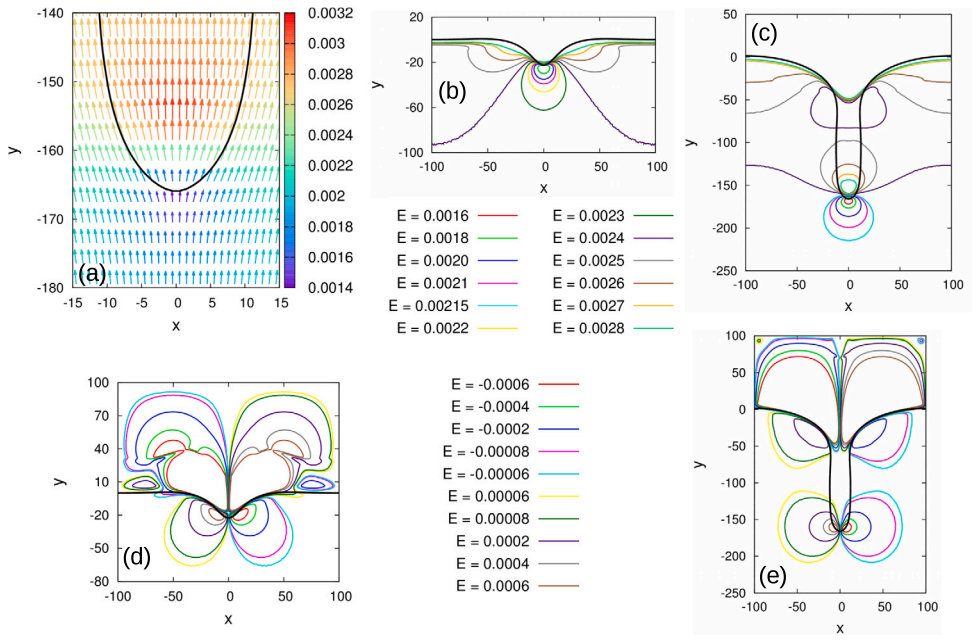

Fig. 6. (a) Distortion of field vectors due to slit formation. Isofield lines of E_y at (b) $t = 10\,000$ and (c) $t = 75\,000$. Phenomenon of field crowding is evident at the root, where an initial monopolar-like arrangement evolves to a dipolar one due to the formation of slit. Isofield lines of E_x at (d) $t = 10\,000$ and (e) $t = 75\,000$. The field lines are symmetric about $x = 0$ and the two slit surfaces carry field of equal magnitude but opposite sign.

categorized as early (Fig. 3(a)), intermediate (Fig. 3(b)) and late stages (Fig. 3(c)).

The early stage is characterized by accelerated grooving, which as compared to the surface diffusion mediated thermal grooves is roughly 5 times deeper at similar timestep. The ridges that emerge at the surface on either side of the GB are less prominent than its thermal groove counterpart. This can be attributed to the fact that unlike matter redistribution from groove root to the surface in thermal grooves, EM-induced flux, in the present case, additionally drains material out of the root. Consequently, the area of the profile representing the net material emerging from the groove is non-zero. It is also worth noting that during the initial stages the change in the slope at the groove root is not evident.

The groove, however, becomes wider and steeper at intermediate times (Fig. 3(b)) and eventually forms a narrow channel-like slit. The trailing edge continues to evolve via surface diffusion as evident from the circular arcs in Fig. 3(c). Once the groove forms a slit-like channel, it propagates along the GB maintaining a constant slit width (distance between the parallel walls). Furthermore, if the profiles at various timesteps are translated such that the slit tip coincides, it can be realized that the slit propagates along the GB self-similarly, preserving its shape near the tip region as observed in Fig. 3(d).

In order to gain deeper insights on the role of surface and GB on slit formation mechanism, we plot the surface (blue arrow) and GB (green arrow) fluxes depicting the direction of diffusion currents. The magnitude of the vector has been upscaled for visual clarity. An enlarged region near the groove root corresponding to early stage $t = 3000$ is shown in Fig. 4(a). Owing to the enhanced mobility the visible diffusion currents are limited to the surface and GB. Moreover, the diffusion currents are restricted along the surface with no visible normal fluxes. Since the GB is planar, essentially all the GB flux (J_{GB}) is EM-induced (J_{GB}^{E}). The surface flux, J_S on the other hand, is an aggregate of two contributions viz. (i) curvature gradient-induced $J_S^{\nabla\kappa_S}$ and (ii) EM-engendered J_S^{E}. It is evident in Fig. 4(a) that the surface and GB fluxes act in tandem in series near the groove root. We consider each of the fluxes in detail one by one.

To understand the direction of $J_S^{\nabla\kappa_S}$ (which is dictated by the gradient of curvature), we calculate the curvature κ_S along the groove profile. The details of the curvature calculation is provided in the appendix. For the sake of comparison, the curvature variation of thermal grooves is also presented in Fig. 5. Thermal grooves are characterized by a convex curvature ($\kappa_S > 0$) with a maximum at the groove root, followed by a decrease leading to diffusion currents out of the groove i.e. from higher curvature to lower curvature. The EM-induced grooves, however, undergo a sign change in the curvature gradient close to the groove root as evident from a steep increase to a maximum followed by a decrease. This prompts $J_S^{\nabla\kappa_S}$ towards the groove root which in general is absent during thermal grooving. Beyond the maximum, there is a reversal in the direction of $J_S^{\nabla\kappa_S}$ which promotes the flattening of the surface ridges as shown in Fig. 4(b). Moreover, with time, the curvature at the groove root (in Fig. 5) exhibits a convex to concave transition, signature of the slit forming tendency of the groove.

Secondly, although the surface is initially perpendicular to the direction of electric field, the development of groove allows a marginal part of the surfaces to come in angular contact with the electron wind. Thus, in addition to $J_S^{\nabla\kappa_S}$, EM-induced surface flux J_S^{E} also instigates a healing flux towards the groove root. It is worth mentioning, that, J_S^{E} at initial stages of grooving is not or rather difficult to account for analytically due to the ever changing shape of the groove cavity. However, as the slit develops, more and more part of the surfaces come in direct line of the electron wind as can be observed in the parallel channel of the slit profile in Fig. 4(c) where κ_S and consequently $J_S^{\nabla\kappa_S}$ is zero. The slit tip region, however, will have contributions from both $J_S^{\nabla\kappa_S}$ and J_S^{E}.

The potential EM-induced damage sites can be assessed by considering the flux divergence. A positive flux divergence implies a net outflux across a closed surface, while a negative value denotes a net influx of matter. The flux divergence plot at two representative timesteps corresponding to Fig. 4(a) and (b) is shown in Fig. 4(d) and (e) respectively. The triple point (surface-GB intersection) can be identified as flux divergence site from the early stages of grooving. The positive region near the root is sustained throughout the slit propagation stage suggesting a higher out going flux J_{GB}^{E} than incoming flux ($J_S^{\nabla\kappa_S} + J_S^{E}$).

Thus, based on the above arguments, it is evident, that contrary to the popular belief, the surface does not act as an independent EM-pathway. Rather, the surface fluxes $J_S^{\nabla\kappa_S}$ and J_S^{E} act as a healing mechanism which replenishes the groove root. However, owing to the

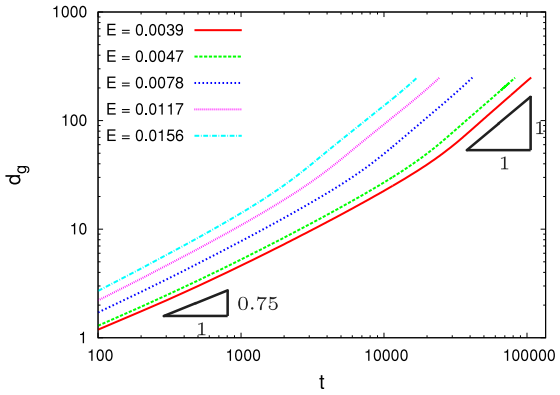

Fig. 7. Temporal evolution of the groove depth (calculated from the initial flat surface) at different applied electric-field strengths plotted on a log–log scale. After an initial power law growth with an exponent of 0.75, a linear regime implying a steady state is attained at all field strengths.

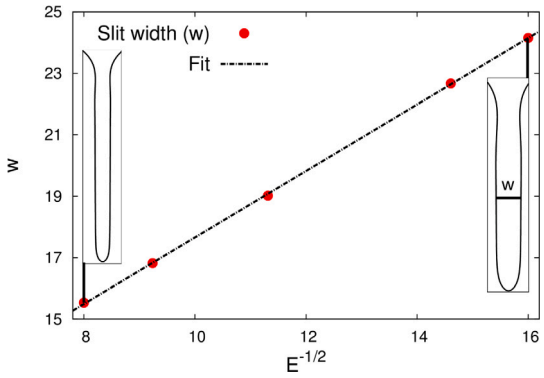

Fig. 8. Dependence of slit width on applied electric-field strengths. Higher field strengths result in narrower slit width selection.

faster mass transport along the GB, J_{GB} is able to localize the groove damage to a slit-like channel and will lead to the phenomenon of slit merging and splitting in a wide polycrystalline line [26].

4.2. Electric field

We next discuss the effect of groove to slit transition on electric field distribution. The formation of slit leads to distortion of field vectors which follow the arc of the slit surface in Fig. 6(a). Electric field contours E_y along the surface contour (solid black line) at two representative timesteps corresponding to intermediate stage $t = 10\,000$ and late stage $t = 75\,000$ are shown in Fig. 6(b) and (c) respectively. Isofield lines follow the groove profile near the top surface at both timesteps and the magnitude decreases as we move further. However, the isofield contours form circular loops (not to be confused with electric field lines which do not form closed loops) with increasing intensity and radius ahead of the groove root. The arrangement is reminiscent of equipotential lines around a monopole (single charge). Furthermore, as the slit develops initial monopolar-like arrangement evolves to a dipolar one near the tip as evident in Fig. 6(b) and (c).

The contours of E_x for similar timesteps are plotted in Fig. 6(d) and (e) Contrary to E_y field strength is maximum near the groove or slit tip and dissipates as we move further along either side of $x = 0$ line. In addition, the field lines are symmetric about $x = 0$ and the slit surfaces carry field of equal magnitude but opposite sign.

A few subtle points also warrants further discussion. Neither E_x nor E_y is constant along the slit surface as is assumed in the analytical calculations of transgranular [13,16] and intergranular slit propagation [22,25], a result consistent with the work of Ouyang and Lee [46] who derived the electric field solution using a conformal mapping technique. Secondly, the isofield lines are more dense near the tip region, a phenomenon known as field crowding. The localized intense field region is known to cause premature electric discharge breakdown in interconnections. Furthermore, isofield lines tend to flatten as they traverse from the interconnect to the underlayer. This is due to the difference in the electrical conductivity of the interconnect which is a metal (higher conductivity) and the underlayer which is a dielectric (lower conductivity).

4.3. Kinetics of groove deepening

The kinetics of the groove extension can be extracted from the displacement of the groove root, measured from the initial flat surface. The position of the groove root is calculated from the minimum value of the ordinate corresponding to $\rho = 0.5$ contour. The resulting displacement–time curve at different applied field strengths is presented in Fig. 7. At initial stages, rate of groove deepening exhibits an exponent of 3/4(0.75) at all field strengths, as evident from the near parallel slopes. The power law kinetics is consistent with expression (10) sans the capillary-induced term. Owing to the lower surface diffusivity selected here, the entity Bt becomes smaller in both the terms in Eq. (10). However, the external flux I which appears as a prefactor, makes the second term dominant as compared to the first term.

It is to be noted that the phase-field simulations differ principally from the analytics on two counts. Firstly, the selected values of γ_{GB} and γ_S in the simulations do no satisfy the small slope approximation (SSA), indicating that the SSA is not restrictive in its scope and in fact serves as an excellent approximation for the early stage behaviour. Moreover, the EM-induced surface flux J_S^E, not accounted for in analytical calculation, plays a minor role during early stages and does not alter the growth exponent.

The 3/4 exponent, however, is not persistent throughout, as the deepening rate increases overtime as apparent from the prerupting of the $d_g - t$ curve. As the groove progressively transits into the slit stage, a linear growth regime, implying a steady state, is attained. The behaviour is observed over a magnitude of electric field. Higher electric field strength results in a sharper and a faster transition to the steady state.

4.4. Selection of slit width and velocity

We next consider the selection of slit width and velocity and its explicit dependence on applied field strength, once the steady state is attained. The slit width is calculated from the difference of the abscissa of the slit profile and averaging the values in the central parallel portion. While, the velocity is extracted from the slope of $d_g - t$ curve (Fig. 7) in linear regime. Higher electric field strengths result in finer slit as seen in Fig. 8. The tip velocity, however, increases with increasing field strength as evident in Fig. 9. Slit width and velocity scales as $E^{-1/2}$ and $E^{3/2}$ respectively which is consistent with the sharp interface description of Klinger et al. [25]and Liu et al. [22] as discussed in Section 2.

It is worth noting that the traditional sharp interface description of the problem approximates the applied electric field E_o by a simple projection along the slit surface $E_o cos\theta$. However, as highlighted in the phase-field simulations (Fig. 6), high curvature at the tip can lead to significant field crowding. Despite the differences in the electric field distribution, the correspondence between sharp interface relation and phase-field simulation is not entirely fortuitous. In fact if we rearrange Eq. (19) we arrive at the width dependence on electric field as, $h = \frac{w}{2} = (\frac{\gamma_S \Omega}{Z_S e E_o A})^{1/2} \propto E_o^{-1/2}$. Similarly, substituting this expression in Eq. (15) and using Eqs. (10) and (11), it can easily be seen that $v \propto E_o^{3/2}$. Thus, the scaling laws arise purely on dimensional grounds independent

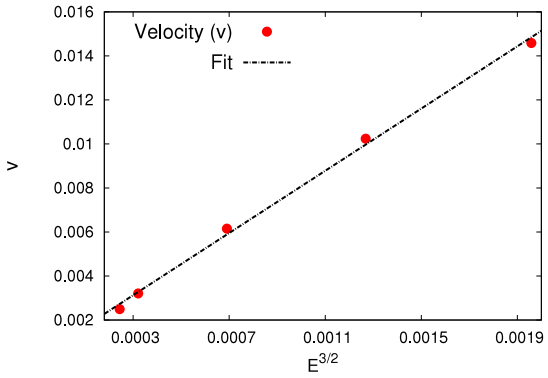

Fig. 9. Dependence of tip velocity on applied field strengths. Higher field strengths result in larger tip velocities.

on the exact solution of laplace equation. Moreover, since higher field leads to narrow slits with smaller tip radius (or in other words higher curvature), the field crowding effect would also be more prominent, thus proving to be more fatal.

4.5. Effect of finite grain size

Since the phase-field simulations allow to track the events leading to slit evolution, the proposition of grain size invariance on slit characteristics can easily be verified. The $d_g - t$ curve corresponding to highest field strength is shown in Fig. 10(a). The initial stages of grooving are almost indiscernible (until $t = 2000$), after which a deviation in the kinetics of deepening can be observed. The variation is significant for the smallest grain. The velocity extracted from the slope of the linear region of the $d_g - t$ curve exhibits a difference of about 25% between the largest and smallest grains.

The above trends can also be argued based on the sharp interface relation. Assuming an infinite slit propagating with a steady state, the tip velocity is dependent on the magnitude of the surface and GB flux remote from the tip through the relation (15). However, during transient stages, when a slit originates from a GB groove, the local flux balance at the tip similar to relation (15) will dictate the tip velocity. For a given magnitude of electric field (and identical conductor length) $J_{GB} = J^E_{GB}$ is constant and independent of grain size, while $J_S = J_S^{\nabla\kappa_S} + J_S^E$ will depend on the curvature of the evolving profile. Groove profiles corresponding to two grain sizes at a similar timestep are shown in Fig. 10(b). Due to smaller grain size, the tails of the neighbouring grooves start overlapping causing the surface to circular arcs. Moreover the trailing edge also undergoes drifting from early stages. In larger grains, the freshly exposed surfaces coming in contact with the electron wind is higher as apparent in Fig. 10(b) such that J_S^E is higher. The curvature variation across the profile is presented in Fig. 10(c). Curvature-gradient $\nabla\kappa_S$ does not change sign in smaller grain implying $J_S^{\nabla\kappa_S}$ along the entire inner surface towards the root. While for larger grain, the curvature-gradient $\nabla\kappa_S$ undergoes a sign change at around $x = 10$ as a result of which $J_S^{\nabla\kappa_S}$ reverses direction. Thus, while the contribution of healing flux from J_S^E is higher for larger grains, $J_S^{\nabla\kappa_S}$ is higher for smaller grains. The flux divergence across the groove profile for the larger and smaller grains is shown in Fig. 10(d) and (e). respectively. Although, in both cases the root exhibits a positive flux change (roughly $J^E_{GB} - (J_S^{\nabla\kappa_S} + J_S^E)$), the magnitude of the change is lower for smaller grains implying a net higher healing flux ($J_S^{\nabla\kappa_S}$ and J_S^E). Healing flux is the precise reason, a slit conceived from a smaller grain will exhibit a slower kinetics and delay damage dissemination. It is worth mentioning that the grain size does not alter the velocity dependence on electric field as evident in Fig. 11(a), but modify only the prefactors resulting in different slopes. However, if we examine the width of the slits emanating from different grain sizes (Fig. 11(b)), the difference is barely perceptible. The slit eventually attains the same shape irrespective of the grain size which is governed by the magnitude of electric field and the dihedral angle.

Another implication of healing flux is that a sufficiently high magnitude of J_S will outweigh J_{GB} as a result of which the breakaway phenomenon of the root will not be observed. Fig. 12(a) depicts the effect of neighbouring grains in suppressing the tendency of slit formation. The magnitude of electric field corresponds to $E = 0.0039$ where slit was observed at larger grain size (Fig. 3). Although the curvature at the root becomes negative during evolution as seen in Fig. 12(b), the concavity is subsequently arrested at a later stage owing to the healing flux. Rather the damage proceeds via a global thinning of the test geometry reminiscent of the Blech-type drift velocity experiments. Such a damage mechanism is expected to be operative at low grain sizes (due to which $J_S^{\nabla\kappa_S}$ and J_S^E will be higher) or at lower J^E_{GB} (either due to lower atomic mobility M_{GB} or applied electric field E). The result can also be interpreted in terms of flux divergence. While intergranular slit results from a localized positive flux divergence at the root (Fig. 4(d) and (e)), overlap of diffusion fields from the neighbouring grains lead to a divergence along the entire surface as seen in Fig. 12(c) and (d) which ensues a surface drift.

4.6. Time to failure

Since most EM tests are performed at accelerated conditions (to speed up the failure process), the results need to be extrapolated to actual service conditions to predict the lifetime of the device. The key parameter of interest is the median-time-to-failure (MTTF) t_f, which exhibits a power law dependence on current density j (or electric field because of their linear dependence due to Ohm's law) according to modified Black's law as [47],

$$t_f = \frac{1}{j^n}\exp\left(\frac{\Delta H}{k_B T}\right), \tag{40}$$

where ΔH is the activation energy for failure. The value of exponent n depends on the rate limiting step of failure. For instance, an exponent of 1 and 2 is associated with the phenomenon of void growth and nucleation respectively [4,48]. Other integral as well as non-integral values have also been reported previously [48,49]. Fractional values of the exponent can be understood by splitting the MTTF into the two distinct stages, namely the time consumed during the nucleation and time elapsed in the growth process. Thus a value of n closer to 1 implies a void growth dominated failure while a slow nucleation phenomenon yields an exponent tending to 2 [48].

Similarly, drawing analogy from the nucleation and growth model, the failure due to intergranular slit can be thought of comprising of two independent processes, the initial grooving stage (t_g) followed by the slit propagation stage (t_p) i.e.,

$$t_f = t_g + t_p \tag{41}$$

Assuming the conductor (GB) length to be L_c and neglecting the capillary-dominated term in Eq. (8), we calculate t_g as,

$$t_g = \frac{1}{B}\left(\frac{\sqrt{2}L_c\Gamma(7/4)}{I}\right)^{4/3} \propto \frac{1}{E^{4/3}} \tag{42}$$

In the slit propagation stage, the velocity exhibits a 3/2 dependence on electric field reading,

$$t_p \propto \frac{1}{E^{3/2}} \tag{43}$$

Thus the exponent in Eq. (40) is anticipated to lie within the range of 1.33 – 1.5.

The time to failure t_f, is extracted from the phase-field simulations as the time taken by the root to translate 85% of the conductor length. The electric field dependence on the time to failure in a double logarithmic plot is presented in Fig. 13. A straight line fit (shown by dashed

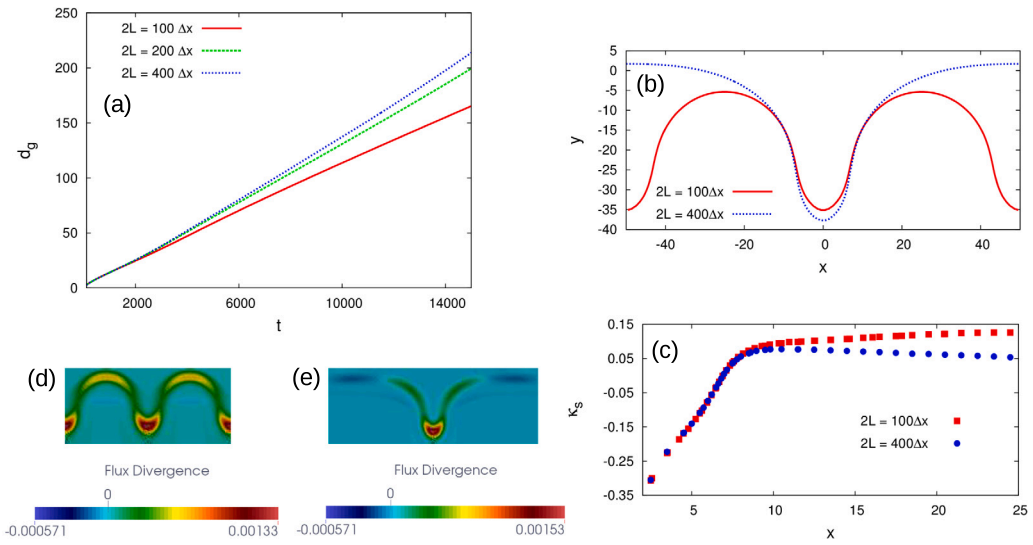

Fig. 10. (a) Temporal evolution of groove depth corresponding to $E = 0.0156$ for different grain sizes. Larger grain leads to faster propagating slit. (b) Comparison of the groove profile at two different grain sizes at $t = 3000$. Smaller grains lead to overlap of tails from neighbouring groove profiles to form circular arcs. (c) Curvature variation along the groove profile corresponding to the groove profiles. Flux divergence along the groove profile for grain size (d) $2L = 100\Delta x$ and (e) $2L = 400\Delta x$. In both the cases the root exhibits a positive flux change ($J_{GB}^{E} - (J_S^{\nabla\kappa_S} + J_S^{E})$), however, the magnitude of the change is lower for smaller grains implying a net higher healing flux ($J_S^{\nabla\kappa_S} + J_S^{E}$).

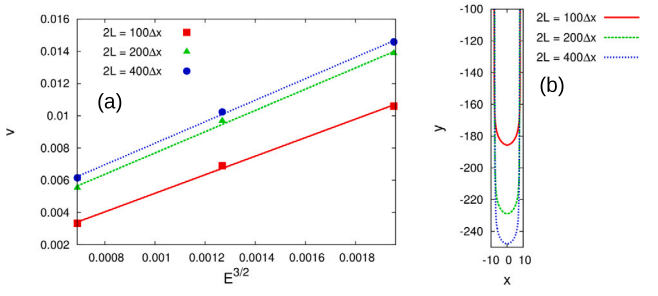

Fig. 11. (a) The variation of steady state tip velocity with electric field for different grain sizes. Although the slit conceived from a smaller grain exhibits slower kinetics, the scaling law is not altered. (b) Slit profile at $t = 17000$ for different grain sizes corresponding to $E = 0.0156$. The slits eventually attain the same shape (slit width) independent of the grain size.

line) yields a slope of $n = 1.33$, suggesting that the initial grooving is the rate controlling step in the failure process. The interpretation is quiet consistent with Fig. 7 where it can be realized that the majority of the time is consumed in attaining the slit shape.

One might however argue that with increasing field strength, the time consumed during the slit advancement will also be significant as evident in Fig. 7 ($E = 0.0156$). As a result the exponent can be expected to shift towards 1.5. A similar prognosis can also be made as the length of the conductor increases. However, it is to be kept in mind that the field strength considered here already corresponds to accelerated conditions. Moreover, with increasing conductor length, the Blech effect [45,50] i.e. the generation of back stresses will retard slit propagation. Therefore, for most practical purposes, the exponent can be presumed to be closer to the lower bound of 1.33 than 1.5.

5. Discussion and concluding remarks

Utilizing a phase-field method, we have explored the viability of GB grooving as a mechanism of origin of intergranular slits. In fact, the phase-field method is able to unify the problems of GB grooving under external effect and intergranular slit propagation which are treated as independent problems in sharp interface description.

The early stages of grooving are described by a power law exponent of 3/4 which is in accordance with the work of Genin et al. [30] and Rosenberg et al. [7]. We mention that both the works considered the evolution of grooves under the influence of external stress with a steady state GB diffusion and SSA assumption, which, in general is valid only at early stages when the change in the GB segment is marginal. GB grooves eventually transit into a narrow channel slit which does not arise under SSA assumed in these works. The slit, thereafter, advances in a steady state by preserving its shape near the tip region as assumed in the work of Klinger et al. [25]. It was further shown in [25] that the steady state solution exists for all values of $M > 1$ in Eq. (20), which also happens to be the case for the numerical parameters selected in the present work.

Our work builds upon the semi-analytical work of Klinger et al. [51] on the effect of GB flux on thermal grooving and emphasizes the role of healing flux not accounted for. The healing surface flux plays an important role during groove to slit transition by replenishing the groove root and delaying slit propagation. This implies that the calculation in Ref. [51] will underestimate the lifetime of interconnect. Another pertinent implication of the healing flux is that it incorporates a grain size dependency on the slit velocity which hitherto has been obscure. Our results suggest that failure can be delayed by about 25% in smaller grains. The scaling laws of slit width and velocity from Ref. [51], however, remain unaffected, because they arise solely on dimensional grounds.

Intergranular slit have been observed in a number of experimental studies [27,52,53]. Narrow slit-like void along GB was reported in Ref. [27,52] in copper interconnects especially in samples with contaminated surface which inhibits surface diffusivity. The activation energy was found to be 0.95 eV using resistance measurement changes during failure phenomenon [52]. The above value is closer to the activation energy of GB diffusion suggesting atomic transport through the GB as rate limiting step. This justifies our choice of atomic mobility values and highlights the role of GB to surface diffusivity ratio in slit formation.

Slit initiating at interconnect-passivation sidewall was reported by Riege et al. [8,53]. Electron wind in such cases is directed along the surface with a component along the tilted GB. The slit originated in form of triangular shaped void similar to Fig. 3(a) in the present study. Shape preserving slit propagation along GB was observed amongst other failure mechanisms. Healing phenomenon was also observed during slit propagation. Insights gained in the present study can easily be extrapolated to explain such damage mechanisms. While J_{GB}^{E} drains

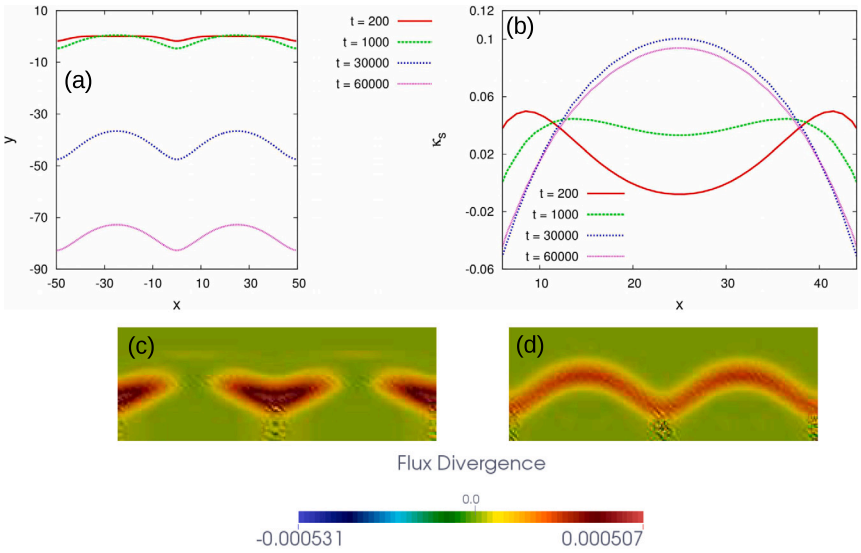

Fig. 12. (a) Groove profile depicting the effect of neighbouring grains in suppressing the tendency of slit formation. (b) Variation of curvature along groove profile. Although, curvature at the root becomes negative, the concavity is arrested subsequently. Flux density map corresponding to timesteps (c) t = 1000 and (d) t = 30 000. Overlapping of neighbouring grains results in a constant surface flux divergence, leading to a homogeneous surface drift.

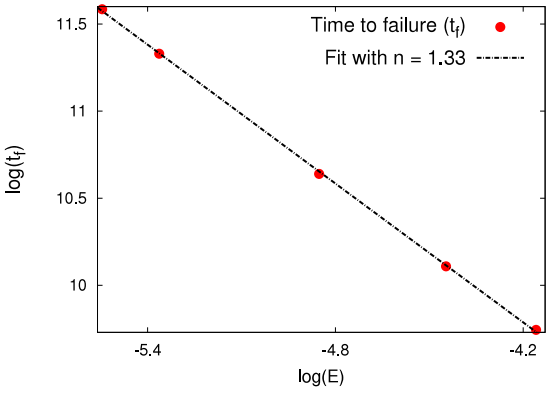

Fig. 13. Electric field dependence on the time to failure on a double logarithmic plot. The time to failure (t_f) is defined as the time taken by the groove tip to translate 85% of the conductor length. A straight line fit yields a slope i.e. an exponent $n = 1.33$ in Black's law Eq. (40).

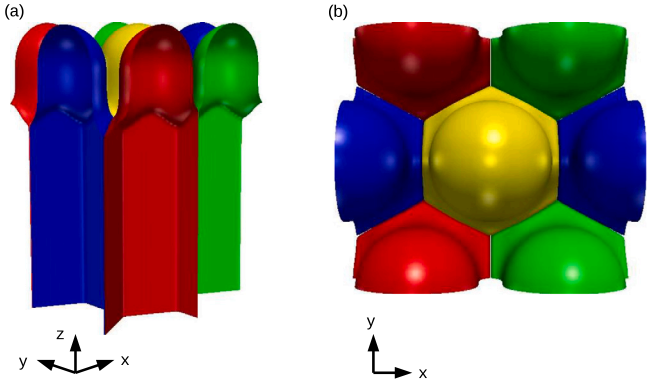

Fig. 14. Three dimensional phase-field simulation depicting intergranular slit propagation at triple junction and grain boundary, (a) side view and (b) top view. Each grain orientation is assigned a different colour. Slit originating at triple junctions appears wider and propagates faster than the ones at grain boundaries. The trailing edge continues to evolve via surface diffusion.

matter from the root, J_S^E heals along one surface and depletes material from the other. Depending upon the curvature variation along the surface, $J_S^{\nabla\kappa_S}$ can also provide an additional healing effect. However, the velocity and width dependence on electric field is expected to be consistent with the present work on dimensional arguments.

The intergranular slit propagation in interconnects also bears a strong resemblance to related phenomenon of cavity growth under applied stress [32,54–56]. Interestingly, surface diffusion limited cavity growth rate also follows a power law dependence on stress (at large stress) with an exponent of 3/2 [54], similar to the present study indicating the universal nature of such problems. As such, most of the scaling laws derived in the present work are anticipated to hold for any intergranular slit whatever be the cause of the external of GB flux. In fact the slit width dependence on electric field ($w \sim E^{-1/2}$) has been recently employed to fabricate nanowires of desired dimensions from a single layer conducting islands on crystalline conducting substrates [57].

A similar groove to slit transition has also been observed in a chemical system by Vogel and Ratke [58] in their experiments concerning Al and Cu bicrystals in contact with In-Al and Bi-Cu melt respectively. A mathematical model extending the theory of thermal grooving revealed GB diffusion of the solute as a source of such instability.

Although we have considered a simple bicrystalline set up, extension of present work to include triple junctions and multiple junctions in a polycrystalline network is straightforward. We close the article with some interesting food for thought. An exemplary simulation of slit formation at triple junction is presented in Fig. 14. A mere visual inspection suggests that the slit emanating at the GB triple junction (TJ) propagates faster than the one at GB. Moreover, the slit at the TJ appears to be wider. This raises the following important concerns regarding the slit manifesting at TJ. How does the slit characteristics at TJ differ from those at GB ? Does the width and velocity scaling laws hold for slit at TJ ? What is the role of healing flux at TJ ? What happens if for a certain magnitude of electric field the slit solution exists at TJ but not at GB ? Such a scenario was already envisaged by Klinger et al. [51] in which they postulated that the trailing edge evolving via surface diffusion will form a bridge resulting in a slit closure. This will result in a transition of a slit to a void advancing along GB. This event is anticipated to repeat successively leading to a relay of migration voids at GB. We look forward to address these compelling problems in

future. In this regard, it is worth mentioning that phase-field method coupled with machine-learning techniques [59–63] can accelerate our understanding of potential failure modes in metal interconnects.

CRediT authorship contribution statement

Arnab Mukherjee: Conceptualization, Methodology, Software, Formal analysis, Writing – original draft. **Kumar Ankit:** Formal analysis, Writing – review & editing. **Michael Selzer:** Software, Writing – review & editing. **Britta Nestler:** Supervision, Funding acquisition, Writing – review & editing.

Declaration of competing interest

The authors declare that they have no known competing financial interests or personal relationships that could have appeared to influence the work reported in this paper.

Data availability

Data will be made available on request.

Acknowledgements

The authors acknowledge the financial support from the ministry of the state Baden-Wuerttemberg through the initiative “Mittelbau”, from the Helmholtz Association, Germany through the project “KIT-Geothermal initiative” within the programme “RE-renewable energies” and from “Bundesministerium fuer Wirtschaft und Energie” within the project “KerSOLife100”.

Appendix. Calculation of the mean curvature

The curvature along the groove profile is defined as the divergence of the normal vector as,

$$\kappa_S = \nabla \cdot \mathbf{n} \tag{A.1}$$

where $\mathbf{n} = \frac{\nabla \rho}{|\nabla \rho|}$. Simplifying the above expression yields,

$$\kappa_S = \frac{\rho_{xx}\rho_y^2 - 2\rho_x\rho_y\rho_{xy} + \rho_{yy}\rho_x^2}{(\rho_x^2 + \rho_y^2)^{3/2}} \tag{A.2}$$

The curvature is calculated along the $\rho = 0.5$ contour. Since these points not necessarily lie on regular lattice points, the location of such points are first calculated from neighbouring two lattice points through a linear interpolation. Following [64], the derivatives are also linearly interpolated from these nearest neighbouring lattice points. The derivatives on the lattice points are discretized using a central finite difference scheme. Thus, the first and second derivatives in the above expression consist information from 4 neighbouring lattice points, while the mixed derivatives from 8 neighbouring lattice points.

References

[1] I. Blech, Electromigration and crevice formation in thin metallic films, Thin Solid Films 13 (1) (1972) 117–129.
[2] P.S. Ho, T. Kwok, Electromigration in metals, Rep. Progr. Phys. 52 (3) (1989) 301.
[3] H. Ceric, S. Selberherr, Electromigration in submicron interconnect features of integrated circuits, Mater. Sci. Eng. R 71 (5) (2011) 53–86.
[4] J. Lloyd, Electromigration failure, J. Appl. Phys. 69 (11) (1991) 7601–7604.
[5] J. Lloyd, Electromigration in integrated circuit conductors, J. Phys. D: Appl. Phys. 32 (17) (1999) R109.
[6] C.-K. Hu, R. Rosenberg, K. Lee, Electromigration path in Cu thin-film lines, Appl. Phys. Lett. 74 (20) (1999) 2945–2947.
[7] R. Rosenberg, M. Ohring, Void formation and growth during electromigration in thin films, J. Appl. Phys. 42 (13) (1971) 5671–5679.
[8] S. Riege, J. Prybyla, A. Hunt, Influence of microstructure on electromigration dynamics in submicron Al interconnects: Real-time imaging, Appl. Phys. Lett. 69 (16) (1996) 2367–2369.
[9] A. Gladkikh, Y. Lereah, E. Glickman, M. Karpovski, A. Palevski, J. Schubert, Hillock formation during electromigration in Cu and Al thin films: Three-dimensional grain growth, Appl. Phys. Lett. 66 (10) (1995) 1214–1215.
[10] Y.-W. Chang, Y. Cheng, F. Xu, L. Helfen, T. Tian, M. Di Michiel, C. Chen, K.-N. Tu, T. Baumbach, Study of electromigration-induced formation of discrete voids in flip-chip solder joints by in-situ 3D laminography observation and finite-element modeling, Acta Mater. 117 (2016) 100–110.
[11] E. Arzt, O. Kraft, W.D. Nix, J. Sanchez Jr., Electromigration failure by shape change of voids in bamboo lines, J. Appl. Phys. 76 (3) (1994) 1563–1571.
[12] O. Kraft, E. Arzt, Electromigration mechanisms in conductor lines: void shape changes and slit-like failure, Acta Mater. 45 (4) (1997) 1599–1611.
[13] M.R. Gungor, D. Maroudas, Theoretical analysis of electromigration-induced failure of metallic thin films due to transgranular void propagation, J. Appl. Phys. 85 (4) (1999) 2233–2246.
[14] Y. Yao, L.M. Keer, M.E. Fine, Electromigration effect on pancake type void propagation near the interface of bulk solder and intermetallic compound, J. Appl. Phys. 105 (6) (2009) 063710.
[15] Y. Yao, Y. Wang, L.M. Keer, M.E. Fine, An analytical method to predict electromigration-induced finger-shaped void growth in SnAgCu solder interconnect, Scr. Mater. 95 (2015) 7–10.
[16] Z. Suo, W. Wang, M. Yang, Electromigration instability: Transgranular slits in interconnects, Appl. Phys. Lett. 64 (15) (1994) 1944–1946.
[17] J. Santoki, A. Mukherjee, D. Schneider, M. Selzer, B. Nestler, Phase-field study of electromigration-induced shape evolution of a transgranular finger-like slit, J. Electron. Mater. 48 (2019) 182–193.
[18] H.-W. Hsueh, F.-Y. Hung, T.-S. Lui, A study on electromigration-inducing intergranular fracture of fine silver alloy wires, Appl. Phys. Lett. 110 (3) (2017) 031902.
[19] M. Mahadevan, R.M. Bradley, Simulations and theory of electromigration-induced slit formation in unpassivated single-crystal metal lines, Phys. Rev. B 59 (16) (1999) 11037.
[20] M. Ohring, Electromigration damage in thin films due to grain boundary grooving processes, J. Appl. Phys. 42 (7) (1971) 2653–2661.
[21] H. Ma, F. La Mattina, I. Shorubalko, R. Spolenak, M. Seita, Engineering the grain boundary network of thin films via ion-irradiation: Towards improved electromigration resistance, Acta Mater. 123 (2017) 272–284.
[22] C.-Y. Liu, S. Lee, T.-j. Chuang, Grain boundary crack growth in interconnects with an electric current, Mater. Sci. Eng. B 86 (2) (2001) 101–108.
[23] J. Santoki, A. Mukherjee, D. Schneider, B. Nestler, Role of conductivity on the electromigration-induced morphological evolution of inclusions in {110}-oriented single crystal metallic thin films, J. Appl. Phys. 126 (16) (2019) 165305.
[24] J. Santoki, A. Mukherjee, D. Schneider, B. Nestler, Effect of conductivity on the electromigration-induced morphological evolution of islands with high symmetries of surface diffusional anisotropy, J. Appl. Phys. 129 (2) (2021) 025110.
[25] L. Klinger, X. Chu, W. Mullins, C. Bauer, Grain-boundary slit propagation in an electric field, J. Appl. Phys. 80 (12) (1996) 6670–6676.
[26] E. Glickman, M. Nathan, On the unusual electromigration behavior of copper interconnects, J. Appl. Phys. 80 (7) (1996) 3782–3791.
[27] N. McCusker, H. Gamble, B. Armstrong, Surface electromigration in copper interconnects, Microelectron. Reliab. 40 (1) (2000) 69–76.
[28] W. Farmer, K. Ankit, Phase-field simulations of electromigration-induced defects in interconnects with non-columnar grain microstructure, J. Appl. Phys. 127 (17) (2020) 175301.
[29] W.W. Mullins, Theory of thermal grooving, J. Appl. Phys. 28 (3) (1957) 333–339.
[30] F. Genin, W. Mullins, P. Wynblatt, The effect of stress on grain boundary grooving, Acta Metall. Mater. 41 (12) (1993) 3541–3547.
[31] P. Martin, Thermal grooving by surface diffusion: Mullins revisited and extended to multiple grooves, Q. Appl. Math. 67 (1) (2009) 125–136.
[32] T.-J. Chuang, J.R. Rice, et al., The shape of intergranular creep cracks growing by surface diffusion, Acta Metall. 21 (12) (1973) 1625–1628.
[33] R. Mukherjee, T. Chakrabarti, E.A. Anumol, T.A. Abinandanan, N. Ravishankar, Thermal stability of spherical nanoporous aggregates and formation of hollow structures by sintering : A phase-field study, ACS Nano 5 (4) (2011) 2700–2706.
[34] Y.U. Wang, Computer modeling and simulation of solid-state sintering: a phase field approach, Acta Mater. 54 (4) (2006) 953–961.
[35] A. Mukherjee, K. Ankit, R. Mukherjee, B. Nestler, Phase-field modeling of grain-boundary grooving under electromigration, J. Electron. Mater. 45 (12) (2016) 6233–6246.
[36] A. Mukherjee, K. Ankit, M. Selzer, B. Nestler, Electromigration-induced surface drift and slit propagation in polycrystalline interconnects: insights from phase-field simulations, Phys. Rev. A 9 (4) (2018) 044004.
[37] I. Blech, E. Kinsbron, Electromigration in thin gold films on molybdenum surfaces, Thin Solid Films 25 (2) (1975) 327–334.
[38] S.M. Allen, J.W. Cahn, A microscopic theory for antiphase boundary motion and its application to antiphase domain coarsening, Acta Metall. 27 (6) (1979) 1085–1095.

[39] J.W. Cahn, J.E. Hilliard, Free energy of a nonuniform system. I. Interfacial free energy, J. Chem. Phys. 28 (2) (1958) 258–267.
[40] P.W. Hoffrogge, A. Mukherjee, E. Nani, P.K. Amos, F. Wang, D. Schneider, B. Nestler, Multiphase-field model for surface diffusion and attachment kinetics in the grand-potential framework, Phys. Rev. E 103 (3) (2021) 033307.
[41] C. Gugenberger, R. Spatschek, K. Kassner, Comparison of phase-field models for surface diffusion, Phys. Rev. E 78 (1) (2008) 016703.
[42] K. Ahmed, T. Allen, A. El-Azab, Phase field modeling for grain growth in porous solids, J. Mater. Sci. 51 (3) (2016) 1261–1277.
[43] A.A. Lee, A. Münch, E. Süli, Sharp-interface limits of the Cahn–Hilliard equation with degenerate mobility, SIAM J. Appl. Math. 76 (2) (2016) 433–456.
[44] A. Mukherjee, Electric Field-Induced Directed Assembly of Diblock Copolymers and Grain Boundary Grooving in Metal Interconnects (Ph.D. thesis), Karlsruher Institut für Technologie (KIT), 2019, http://dx.doi.org/10.5445/IR/1000096625.
[45] I.A. Blech, Electromigration in thin aluminum films on titanium nitride, J. Appl. Phys. 47 (4) (1976) 1203–1208.
[46] H. Ouyang, S. Lee, Application of linear elastic fracture mechanics on electric discharge breakdown in interconnects, Appl. Phys. Lett. 73 (24) (1998) 3565–3567.
[47] J.R. Black, Electromigration failure modes in aluminum metallization for semiconductor devices, Proc. IEEE 57 (9) (1969) 1587–1594.
[48] J. Lloyd, Black's law revisited—Nucleation and growth in electromigration failure, Microelectron. Reliab. 47 (9) (2007) 1468–1472.
[49] Y. Wang, Y. Yao, A theoretical analysis to current exponent variation regularity and electromigration-induced failure, J. Appl. Phys. 121 (6) (2017) 065701.
[50] I. Blech, K. Tai, Measurement of stress gradients generated by electromigration, Appl. Phys. Lett. 30 (8) (1977) 387–389.
[51] L. Klinger, E. Glickman, V. Fradkov, W. Mullins, C. Bauer, Extensions of thermal grooving for arbitrary grain-boundary flux, J. Appl. Phys. 78 (6) (1995) 3833–3838.
[52] A. Gladkikh, M. Karpovski, A. Palevski, Y.S. Kaganovskii, Effect of microstructure on electromigration kinetics in Cu lines, J. Phys. D: Appl. Phys. 31 (14) (1998) 1626.
[53] S. Riege, A. Hunt, J. Prybyla, Real-time TEM studies of electromigration in submicron aluminum runners, in: MRS Proceedings, Vol. 391, Cambridge Univ Press, 1995, p. 249.
[54] T.-J. Chuang, K.I. Kagawa, J.R. Rice, L.B. Sills, Overview no. 2: Non-equilibrium models for diffusive cavitation of grain interfaces, Acta Metall. 27 (3) (1979) 265–284.
[55] G. Pharr, W. Nix, A numerical study of cavity growth controlled by surface diffusion, Acta Metall. 27 (10) (1979) 1615–1631.
[56] A. Needleman, J. Rice, Plastic creep flow effects in the diffusive cavitation of grain boundaries, Acta Metall. 28 (10) (1980) 1315–1332.
[57] A. Kumar, D. Dasgupta, C. Dimitrakopoulos, D. Maroudas, Current-driven nanowire formation on surfaces of crystalline conducting substrates, Appl. Phys. Lett. 108 (19) (2016) 193109.
[58] H. Vogel, L. Ratke, Instability of grain boundary grooves due to equilibrium grain boundary diffusion, Acta Metall. Mater. 39 (4) (1991) 641–649.
[59] A.S. Iquebal, P. Wu, A. Sarfraz, K. Ankit, Emulating the evolution of phase separating microstructures using low-dimensional tensor decomposition and nonlinear regression, MRS Bull. (2023) 1–12.
[60] P. Wu, W. Farmer, A. Iquebal, K. Ankit, A novel data-driven emulator for predicting electromigration-mediated damage in polycrystalline interconnects, J. Electron. Mater. (2023) 1–16.
[61] A. Kunwar, Y.A. Coutinho, J. Hektor, H. Ma, N. Moelans, Integration of machine learning with phase field method to model the electromigration induced Cu6Sn5 IMC growth at anode side Cu/Sn interface, J. Mater. Sci. Technol. 59 (2020) 203–219.
[62] D. Montes de Oca Zapiain, J.A. Stewart, R. Dingreville, Accelerating phase-field-based microstructure evolution predictions via surrogate models trained by machine learning methods, Npj Comput. Mater. 7 (1) (2021) 3.
[63] K. Yang, Y. Cao, Y. Zhang, S. Fan, M. Tang, D. Aberg, B. Sadigh, F. Zhou, Self-supervised learning and prediction of microstructure evolution with convolutional recurrent neural networks, Patterns 2 (5) (2021) 100243.
[64] W.T. Góźdź, R. Hołyst, Triply periodic surfaces and multiply continuous structures from the Landau model of microemulsions, Phys. Rev. E 54 (5) (1996) 5012.